






















# On the evolution of the Anisotropic Scaling of Magnetohydrodynamic Turbulence in the Inner Heliosphere.

NIKOS SIOULAS <sup>1</sup> MARCO VELLI <sup>1, 2</sup> ZESSEN HUANG (黄泽森) <sup>1</sup> CHEN SHI (时辰) <sup>1</sup>  
TREVOR A. BOWEN <sup>3</sup> B. D. G. CHANDRAN <sup>4</sup> IOANNIS LIODIS <sup>5</sup> STUART D. BALE <sup>6, 7</sup>  
T. S. HORBURY <sup>8</sup> THIERRY DUDOK DE WIT <sup>9</sup> DAVIN LARSON <sup>7</sup> JUSTIN KASPER <sup>10, 11</sup>  
CHRISTOPHER J. OWEN <sup>12</sup> MICHAEL L. STEVENS <sup>13</sup> ANTHONY CASE <sup>14</sup> MARC PULUPA <sup>7</sup>  
J.W. BONNELL <sup>7</sup> ROBERTO LIVI <sup>7</sup> KEITH GOETZ <sup>15</sup> PETER R. HARVEY <sup>7</sup> AND  
ROBERT J. MACDOWALL <sup>16</sup>

<sup>1</sup>*Department of Earth, Planetary, and Space Sciences, University of California, Los Angeles  
Los Angeles, CA 90095, USA*

<sup>2</sup>*International Space Science Institute, 3012 Bern Switzerland*

<sup>3</sup>*Space Sciences Laboratory, University of California,  
Berkeley, CA 94720-7450, USA*

<sup>4</sup>*Space Science Center, University of New Hampshire, Durham, NH 03824, USA*

<sup>5</sup>*Deptment of Physics, Aristotle University of Thessaloniki  
GR-52124 Thessaloniki, Greece*

<sup>6</sup>*Physics Department, University of California, Berkeley, CA 94720-7300, USA*

<sup>7</sup>*Space Sciences Laboratory, University of California, Berkeley, CA 94720-7450, USA*

<sup>8</sup>*The Blackett Laboratory, Imperial College London, London, UK*

<sup>9</sup>*LPC2E, CNRS and University of Orléans, Orléans, France*

<sup>10</sup>*BWX Technologies, Inc., Washington DC 20002, USA*

<sup>11</sup>*Climate and Space Sciences and Engineering, University of Michigan, Ann Arbor, MI 48109, USA*

<sup>12</sup>*Mullard Space Science Laboratory, University College London, Dorking, RH5 6NT, UK*

<sup>13</sup>*Harvard-Smithsonian Center for Astrophysics,  
Cambridge, MA 02138, USA*

<sup>14</sup>*Smithsonian Astrophysical Observatory,  
Cambridge, MA 02138, US*

<sup>15</sup>*School of Physics and Astronomy, University of Minnesota, Minneapolis, MN 55455, USA*

<sup>16</sup>*Solar System Exploration Division, NASA/Goddard Space Flight Center, Greenbelt, MD, 20771*

## ABSTRACT

We analyze a merged Parker Solar Probe (*PSP*) and Solar Orbiter (*SO*) dataset covering heliocentric distances  $13 R_{\odot} \lesssim R \lesssim 220 R_{\odot}$  to investigate the radial evolution of power and spectral-index anisotropy in the wavevector space of solar wind turbulence. Our results show that anisotropic signatures of turbulence display a distinct radial evolution when fast,  $V_{sw} \geq 400 \text{ km s}^{-1}$ , and slow,  $V_{sw} \leq 400 \text{ km s}^{-1}$ , wind streams are considered. The anisotropic properties of slow wind in Earth orbit are consistent with a “critically balanced” cascade, but both spectral-index anisotropy and power

anisotropy diminish with decreasing heliographic distance. Fast streams are observed to roughly retain their near-Sun anisotropic properties, with the observed spectral index and power anisotropies being more consistent with a “dynamically aligned” type of cascade, though the lack of extended fast-wind intervals makes it difficult to accurately measure the anisotropic scaling. A high-resolution analysis during the first perihelion of PSP confirms the presence of two sub-ranges within the inertial range, which may be associated with the transition from weak to strong turbulence. The transition occurs at  $\kappa d_i \approx 6 \times 10^{-2}$ , and signifies a shift from -5/3 to -2 and -3/2 to -1.57 scaling in parallel and perpendicular spectra, respectively. Our results provide strong observational constraints for anisotropic theories of MHD turbulence in the solar wind.

*Keywords:* Parker Solar Probe, Solar Orbiter, Solar Wind, Anisotropic MHD Turbulence

## 1. INTRODUCTION

Magnetohydrodynamic (MHD) turbulence is relevant to a wide range of astrophysical systems such as stellar coronae, stellar winds, and the interstellar medium. A large-scale magnetic field  $\mathbf{B}_0$ <sup>1</sup> is often present (Parker 1979; Biskamp 2003) and the fluctuations are typically observed to be mostly incompressible. The incompressible MHD equations are better expressed using Elsasser variables,  $\mathbf{z}^\pm = \mathbf{v} \pm \mathbf{b}$  (Elsasser 1950), where the nonlinear term for each variable may be written  $\partial_t \mathbf{z}^\pm \sim -\mathbf{z}^\mp \cdot \nabla \mathbf{z}^\pm$  (here  $\sim$  means proportional up to a projection operator ensuring incompressibility): nonlinear effects therefore require interactions between fluctuations with opposite signs of cross-helicity. Based on the weak interaction of oppositely moving Alfvénic wavepackets in a strong background magnetic field,  $\delta v, \delta b \ll B_0$ , i.e., assuming that the wave propagation,  $\tau_A(\boldsymbol{\kappa}) = 1/|\mathbf{B} \cdot \mathbf{k}|$  is shorter than the nonlinear decay time  $\tau_{nl}(\boldsymbol{\kappa}) \approx 1/(k \cdot \delta u_k)$ , where  $\delta u_k$  is the average velocity fluctuation at scales  $\ell \sim 1/|\mathbf{k}|$ , the turbulent cascade will be slowed relative to hydrodynamic turbulence (Iroshnikov 1963; Kraich-

nan 1965). Assuming homogeneity, isotropy,  $\mathbf{B} \cdot \mathbf{k} \rightarrow B \cdot k$ , and scale locality of the interactions, simple dimensional analysis then leads to the prediction of the inertial range omnidirectional power-spectrum,  $E(k) \propto k^{-3/2}$ . Magnetic fields, however, cannot be eliminated via Galilean transformations of MHD equations, as opposed to mean velocity fields,  $\mathbf{V}_0$ , resulting in strongly anisotropic turbulent dynamics (Montgomery & Turner 1981) (see also reviews by Schekochihin et al. 2009; Oughton et al. 2015, and references therein). In particular, conservation of energy and momentum during wave-wave interactions (more specifically, a wave - 2D perturbation interaction, (see, Montgomery & Matthaeus 1995)) allows power to cascade down to smaller scales perpendicular to  $\mathbf{B}_0$ , resulting in a two-dimensionalization of the turbulence spectrum in a plane transverse to the locally dominant magnetic field while at the same time inhibiting spectral energy transfer along the direction parallel to the field. (Shebalin et al. 1983; Ng & Bhattacharjee 1996; Galtier et al. 2000).

A multitude of observational and numerical studies have investigated the manifestations of anisotropy in the presence of an energetically significant mean magnetic field e.g., anisotropy

<sup>1</sup> Magnetic fields are presented in Alfvén velocity units, e.g.,  $\mathbf{b} \rightarrow \mathbf{b}/\sqrt{4\pi\rho}$ ,  $\mathbf{B}_0 \equiv \mathbf{V}_a$

in correlation functions, power at a fixed scale, spectral indices, intermittency

(Belcher & Davis Jr. 1971; Matthaeus et al. 1990; Bieber et al. 1996; Maron & Goldreich 2001; Weygand et al. 2009; Beresnyak & Lazarian 2010; Osman et al. 2012; Wicks et al. 2013; Chandran & Perez 2019; Pine et al. 2020; Bandyopadhyay & McComas 2021; Zank et al. 2022; Sioulas et al. 2022a; Chhiber 2022; Dong et al. 2022). A comprehensive overview of the various forms of anisotropy can be found in Horbury et al. (2012)

The dependence of the inertial range power-spectral index,  $\alpha_B$ , on the field/flow angle,  $\Theta_{BV}$ , where  $\mathbf{B}_0^{loc}$  (hereafter referred to as  $\mathbf{B}$ ) is a local, scale-dependent mean magnetic field, has been investigated using wavelet techniques by (Horbury et al. 2008; Podesta 2009; Chen et al. 2011). These studies suggest that the magnetic power-law indices were  $-2$  and  $-5/3$  in flow directions parallel ( $\Theta_{BV} \approx 0^\circ$ ) and perpendicular ( $\Theta_{BV} \approx 90^\circ$ ) to the mean magnetic field, respectively. These observations were interpreted as supporting evidence for the *critical balance* (CB) theory (Sridhar & Goldreich 1994; Goldreich & Sridhar 1995, 1997)<sup>2</sup>, which is based on the conjecture that the inertial range dynamics of MHD turbulence with vanishing cross-helicity ( $\sigma_c \approx 0$ ), later extended to imbalanced cascades (Lithwick et al. 2007), are governed by wavevector modes for which rough equality between  $\tau_A(\boldsymbol{\kappa})$  and  $\tau_{nl}(\boldsymbol{\kappa})$ ,  $\tau_A(\mathbf{k}) \approx \tau_{nl}(|\mathbf{k}|)$  holds. As a result, the relationship between the parallel and perpendicular wavevectors follows an anisotropic scaling,  $\kappa_{||} \sim \kappa_{\perp}^{2/3}$ . Based on this scaling, we expect the magnetic fluctuation spectra to follow scalings of:  $E(k_{\perp}) \propto k_{\perp}^{-5/3}$  and  $E(k_{||}) \propto k_{||}^{-2}$ . However, the *dynamic alignment* conjecture (Boldyrev 2006; Mason et al. 2006; Perez & Boldyrev 2009) suggests that, as the energy cascades to smaller scales, velocity and

magnetic field fluctuations in the plane perpendicular to  $\mathbf{B}_0$  will align to within a smaller angle  $\phi$ , resulting in weaker nonlinear interactions and a flatter perpendicular inertial range spectrum,  $E(k_{\perp}) \propto k_{\perp}^{-3/2}$ .

Recent observations from the Parker Solar Probe (PSP) and Solar Orbiter (SO) missions have provided the opportunity to investigate the radial evolution of turbulence in the inner heliosphere. It was shown that the inertial range of the magnetic spectrum grows with distance, progressively extending to larger spatial scales (Sioulas et al. 2022b) while at the same time steepening from a scaling of  $\alpha_B = -3/2$  at approximately 0.06 au towards the Kolmogorov scaling of  $\alpha_B = -5/3$  (Chen et al. 2020; Alberti et al. 2020; Telloni et al. 2021; Shi et al. 2021). The rate at which the spectrum steepens has also been found to be related to the Alfvénic content and magnetic energy excess of the fluctuations (Sioulas et al. 2022b). On the contrary, the spectral index of the velocity spectrum in the inertial range has consistently been found to be close to  $\alpha_v = -3/2$ , regardless of the distance from the Sun (Shi et al. 2021).

In this study, we aim to understand the radial evolution of anisotropic magnetic turbulence in the inner heliosphere. To do this, we analyze data from the PSP and SO missions covering heliocentric distances  $13 R_{\odot} \lesssim R \lesssim 220 R_{\odot}$  using wavelet analysis. This technique allows us to decompose the magnetic field timeseries into scale-dependent background and fluctuations, and study the dependence of the turbulence properties on the field/flow angle  $\theta_{BV}$ .

The rest of the paper is structured as follows: In Section 2, we provide background on wavelet analysis and introduce the anisotropy diagnostics used in this study. Section 3 presents the selection and processing of the data. The results of this study are presented in Section 4, with a focus on high-resolution data obtained during the first perihelion of PSP in Subsection 4.1, and

<sup>2</sup> Heavily influenced by the work of Higdon (1984).

the radial evolution of magnetic field anisotropy investigated in Subsection 4.2. In Section 6, we compare our findings to previous relevant studies in order to advance our understanding of the topic and validate our conclusions. The discussion of the results and conclusions are provided in Sections 5 and 7, respectively.

## 2. BACKGROUND

### 2.1. Wavelet analysis & estimation of Power Spectral Density (PSD)

Anisotropy in turbulence is a local property that depends on both position and scale. Turbulent fluctuations at a given scale,  $\ell$ , are strongly affected by the local mean magnetic field of size  $3 - 5 \cdot \ell$  (Gerick et al. 2017). Wavelet analysis is a useful technique for studying anisotropy because it enables the decomposition of a signal into components that are localized in both time and wavelet scale. In recent years, the continuous wavelet transform (CWT) has been widely used to estimate the power of magnetic field fluctuations as a function of the direction of the local mean magnetic field (Podesta 2009; Wicks et al. 2010). For a discrete set of measurements, such as the time series of the  $i$ -th component of the magnetic field,  $B_i$ ,  $i = R, T, N$  with a resolution of  $\delta t$ , the wavelet transform can be implemented as follows:

$$\omega_i(\ell, t_n) = \sum_{j=0}^{N-1} B_i(t_j) \psi^*\left(\frac{t_j - t_n}{\ell}\right), \quad (1)$$

where  $\psi^*$  is conjugate of the Morlet mother wavelet,  $\psi(t) = \pi^{-1/4} [e^{i\omega_0 t} - e^{-\frac{\omega_0^2}{2}}] e^{-\frac{t^2}{2}}$ , and  $\omega_0$  is an adjustable parameter that represents the frequency of the wavelet and is set equal to  $\omega_0 = 6$ . The transformation from the dilation scale,  $\ell$ , to the physical spacecraft frequency,  $f_{sc}$ , is given by:

$$f_{sc} = \frac{\omega_0}{2\pi \Delta t \ell}, \quad (2)$$

where  $\Delta t$  denotes the time interval between successive measurements. The power spectral density of the  $i$ -th component as a function of spacecraft frequency  $f_{sc}$  and the local, scale-dependent field/flow angle  $\theta_{BV}$  can be estimated as

$$F_{ii}(f_{sc}, \theta_{BV}) = \frac{2\delta t}{N} \sum_{n=0}^{N-1} |\omega_i(\ell, t_n, \theta_{BV})|^2, \quad (3)$$

where,  $N$  is the number of times for which  $\theta_{j-1} \leq \theta_{BV} \leq \theta_j$ ,  $\theta_j = 5^\circ \cdot j$ , where,  $j=0, 1, \dots, 18$ . Based on the symmetry of  $\theta_{BV}$  about  $90^\circ$ , we restricted the range of  $\theta_{BV}$  to be between  $0^\circ$  and  $90^\circ$ . In the subsequent analysis, we examined the trace of the power spectral density,  $F = \sum F_{ii}$ .

The local mean magnetic field direction at time  $t_n$  and wavelet scale  $\ell$  can be estimated by weighting the magnetic field time series with a Gaussian curve centered at  $t_n$  as follows:

$$\bar{B}_n(t_n, \ell) = \sum_{m=0}^{N-1} B_m \exp\left[-\frac{(t_n - t_m)^2}{2\lambda^2 \ell^2}\right], \quad (4)$$

where the width of the scaled Gaussian curve is  $2^{3/2} \lambda \ell \approx 2.8 \lambda \ell$ , and  $\lambda$  is a dimensionless parameter that determines the scale of the average and is set equal to 1. To further validate the robustness of our results, we repeated the analysis with  $\lambda = 3$ . We found that the results were highly comparable to those obtained with  $\lambda = 1$ , with spectral exponents differing by only 0.01-0.02.

To convert the spacecraft-frame frequency derived PSD,  $F(f_{sc}, \theta_{BV})$  into a wavenumber spectrum expressed in physical units  $E(\kappa^*, \theta_{BV})$ , we implement a modified version of Taylor's hypothesis (Taylor 1938) that accounts for wave propagation as well as the spacecraft velocity (Klein et al. 2015):

$$E(\kappa^*, \theta_{BV}) = \frac{V_{tot}}{2\pi \cdot d_i} F(f_{sc}, \theta_{BV}) [nT^2 \cdot d_i], \quad (5)$$

where,  $\kappa^* = \kappa \cdot d_i = 2\pi f_{sc}/V_{tot} \cdot d_i$ ,  $d_i$  is the ion inertial length,  $V_{tot} = |\mathbf{V}_{sw} + \mathbf{V}_a - \mathbf{V}_{sc}|$ , and  $\mathbf{V}_{sc}$  is the spacecraft velocity.

### 3. DATA SELECTION AND PROCESSING

#### 3.1. Data Selection

As a first step, observations of PSP between January 1, 2018, and October 1, 2022, were collected, encompassing the first thirteen perihelia (E1 – E13) of the PSP mission. Level 2 magnetic field data from the Flux Gate Magnetometer (FGM) (Bale et al. 2016), as well as Level 3 plasma moment data from the Solar Probe Cup (SPC) for E1-E8, and the Solar Probe Analyzer (SPAN) from the Solar Wind Electron, Alpha and Proton (SWEAP) suite for E9-E13 (Kasper et al. 2016), were analyzed. Data from the SCaM product (Bowen et al. 2020) obtained during E1 have also been analyzed and will be presented as a high-quality case study. The plasma data consists of moments of the distribution function computed on board the spacecraft, including the proton velocity vector  $\mathbf{V}_p$ , number density  $n_p$ , and temperature  $T_p$ . When available, electron number density data derived from the quasi-thermal noise from the FIELDS instrument (Moncuquet et al. 2020) were preferred over SPAN or SPC data for estimating proton number density. In order to calculate the proton density from the electron density, charge neutrality must be considered, leading to a  $\approx 4\%$  abundance of alpha particles. Therefore, electron density from QTN was divided by 1.08.

The second step involved obtaining magnetic field and particle measurements from the SO mission between June 1, 2018, to March 1, 2022. Magnetic field measurements from the Magnetometer (MAG) instrument (Horbury et al. 2020). Note, that burst magnetic field data have been utilized when available. Particle moments measurements for our study are provided by the Proton and Alpha Particle Sensor (SWA-PAS)

onboard the Solar Wind Analyser (SWA) suite of instruments (Owen et al. 2020).

#### 3.2. Data processing

Quality flags for the magnetic field and particle time series have been taken into account, and time intervals missing  $\geq 1\%$  and/or  $\geq 10\%$  in the magnetic field and particle time series have been omitted from further analysis. Additionally, the mean value of the cadence between successive measurements  $\delta\tau$  in the magnetic field time series has been estimated for each of the selected intervals, and time intervals that were found to have a mean cadence of  $\delta\tau \geq 250$  ms were discarded. Due to poor data quality, all PSP intervals exceeding  $R \simeq 0.5$  au have also been discarded.

Spurious spikes in the plasma time series were eliminated by replacing outliers exceeding three standard deviations within a moving average window covering 200 points with their median values (Davies & Gather 1993).

## 4. RESULTS

#### 4.1. Case Study: SCaM Dataset, E1

The high-resolution data from the first perihelion of the PSP ( $R \approx 0.17$  au) from November 1 to November 11, 2018, was analyzed. A total of 33 intervals with a duration of 12 hours were obtained and the power spectral density was estimated, with subsequent intervals overlapping by 50%. The analysis covered 18 bins of the  $\theta_{BV}$  angle, but in the following, we will only focus on those bins closer to the parallel and perpendicular directions, with  $\theta_{BV} \leq 5^\circ$  and  $\theta_{BV} \geq 85^\circ$ , respectively. It is worth noting that the second half of E1 displayed significantly different characteristics compared to the first half, with the solar wind exhibiting higher speeds and a greater number of magnetic switchbacks (Bale et al. 2019). It is well established that power spectra exhibit different characteristics when different solar wind speeds are considered due



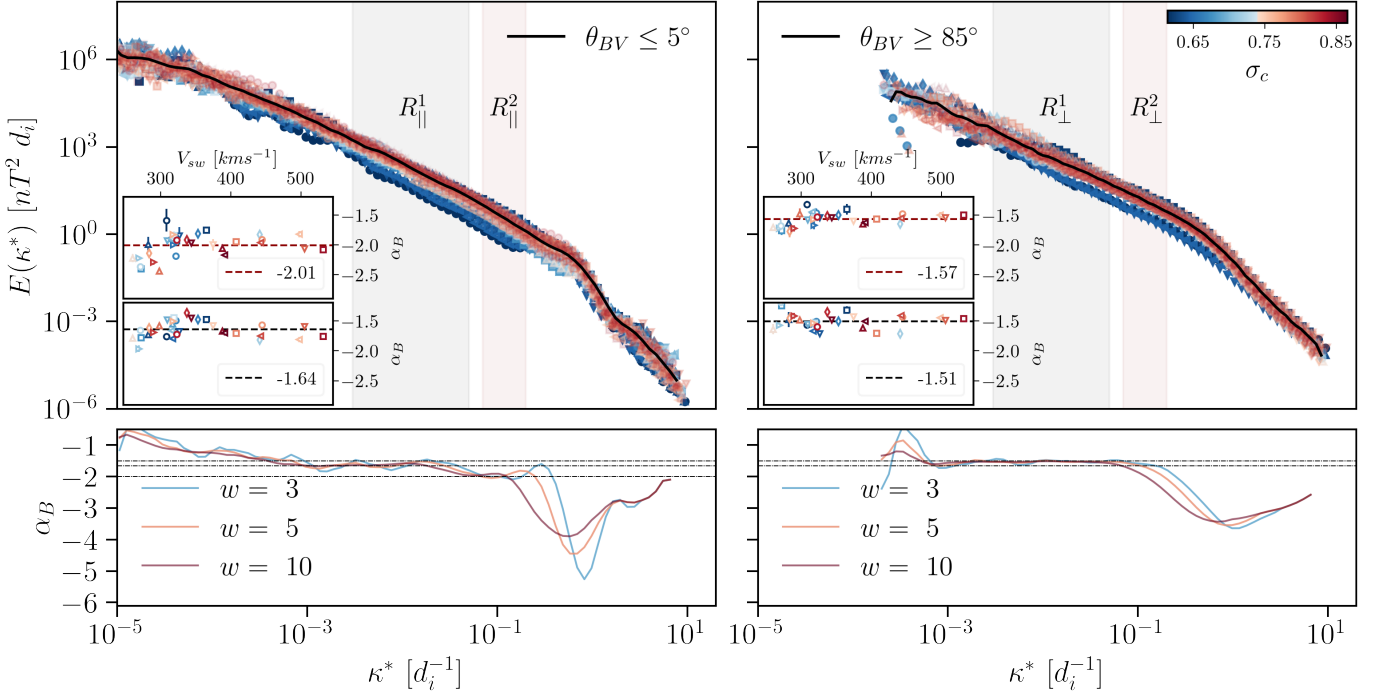


**Figure 1.** Averaged magnetic field power-spectrum (black solid line) for fluctuations parallel  $\theta_{BV} \leq 5^\circ$  (left panel) and perpendicular  $\theta_{BV} \geq 85^\circ$  (right panel) to the local magnetic field during the first perihelion of PSP (E1) estimated using SCAm data. The dependence of the spectra on normalized cross-helicity ( $\sigma_c$ ) is also shown, with the color keyed to  $\sigma_c$ . The inset figures illustrate the spectral index  $\alpha_B$ , at two different ranges of scales (bottom)  $3 \times 10^{-3} - 5 \times 10^{-2} d_i$  and (top)  $8 \times 10^{-2} - 2 \times 10^{-1} d_i$  as a function of solar wind speed and  $\sigma_c$ . The dashed horizontal lines indicate the mean value of  $\alpha_B$ . The second row illustrates the local  $\alpha_B$ , calculated over a sliding window of a factor of 3, 5, and 10 shown in cyan, orange, and red respectively. Horizontal dotted lines have also been added marking values  $-3/2$ ,  $-5/3$  and  $-2$

to the different types of fluctuations they transport (Borovsky et al. 2019). Specifically, the fast solar wind is highly Alfvénic and characterized by large-amplitude, incompressible fluctuations, while the slow wind is generally populated by smaller amplitude, less Alfvénic, compressive fluctuations (Bruno et al. 2003; Matteini et al. 2014; Shi et al. 2021; Sioulas et al. 2022a). Consequently, the spectral variation due to the differing plasma parameters of the selected streams was investigated. More specifically, we considered the dependence of the PSD on the solar wind speed,  $V_{sw}$ , the normalized cross helicity  $\sigma_c$ :

$$\sigma_c = \frac{E_o - E_i}{E_o + E_i}, \quad (6)$$

a measure of the relative amplitudes of inwardly and outwardly propagating Alfvén waves, and the normalized residual energy  $\sigma_r$ :

$$\sigma_r = \frac{E_V - E_b}{E_V + E_b}, \quad (7)$$

indicating the balance between kinetic and magnetic energy, where,  $E_q = \frac{1}{2} \langle \delta \phi^2 \rangle$  denotes the energy associated with the fluctuations of the field  $\phi$ . In particular,  $E_{o,i}$  can be estimated using Elsasser variables, defining outward and inward propagating Alfvénic fluctuations (Velli et al. 1991; Velli 1993)

$$\delta \mathbf{Z}_{o,i} = \delta \mathbf{V} \mp \text{sign}(B_0^R) \delta \mathbf{b}, \quad (8)$$

$\delta \mathbf{B} = \mathbf{B} - \mathbf{B}_0$ ,  $\mathbf{B}_0$  the background magnetic field,  $\delta \mathbf{b} = \delta \mathbf{B} / \sqrt{\mu_0 m_p n_p}$  the magnetic fluctuations in Alfvén units and  $B_0^R$  the ensemble aver-

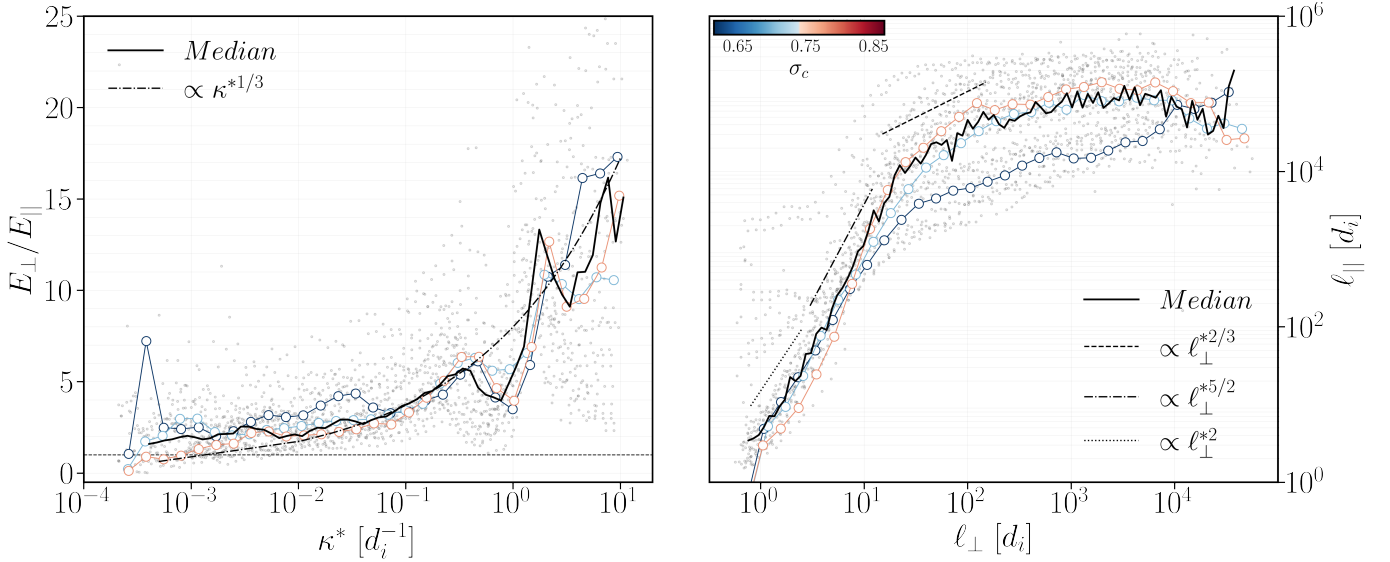


**Figure 2.** (a) The anisotropy of the fluctuations described by the ratio of the perpendicular ( $E_{\perp}$ ) to the parallel power ( $E_{\parallel}$ ). A horizontal black solid line has been added to indicate  $E_{\perp}/E_{\parallel} = 1$ . (b) The relation between  $\ell_{\parallel}$  and  $\ell_{\perp}$ , interpreted as wavevector anisotropy. In both cases, intervals have also been binned based on their  $\sigma_c$  value. The median curve for each bin is shown with the color of each curve keyed to  $\sigma_c$ .

age of  $B_R$ , utilized to determine the polarity of the radial magnetic field (Shi et al. 2021). The magnetic field power-spectrum for fluctuations parallel  $\theta_{BV} \leq 5^\circ$  and perpendicular  $\theta_{BV} \geq 85^\circ$  to the local magnetic field, resulting from averaging all the respective spectra are presented in Figure 1. Individual spectra are also shown with the color of the curve keyed to  $\sigma_c$ . The fluctuation power in the MHD range shows a positive correlation with  $\sigma_c$ , but this dependence vanishes in the transition region and kinetic scales. A similar trend was observed with  $\sigma_r$  and  $V_{sw}$ , not shown here. The results are consistent with (Vasquez et al. 2007), who found higher, MHD range, turbulence amplitudes associated with faster streams, as well as, (Pi et al. 2020) who showed that such dependence vanishes in the kinetic scales. The trend also vanishes at the large, energy injection scales,  $\kappa d_i \leq 10^{-3}$ , where the power spectrum is clearly dominated by parallel fluctuations. Focusing our attention on MHD scales, we can observe two distinct ranges, roughly  $3 \times 10^{-3} - 5 \times 10^{-2} \kappa d_i$  and  $8 \times 10^{-2} - 2 \times 10^{-1} \kappa d_i$ , over which the PSD displays a clear power-law scaling. A light-black

and red shade are used to indicate these regions in the figure, and we will thereby refer to them as  $R_{\parallel(\perp)}^1$ , and  $R_{\parallel(\perp)}^2$ . The power-law fitting has been applied to the PSD for the two ranges, and the bottom and top inset figures illustrate  $\alpha_B$  as a function of  $V_{sw}$ . Note, that the color of the scatter plot is keyed to  $\sigma_c$ . Furthermore, horizontal lines have been added to indicate the average value of  $\alpha_B$ . In the direction parallel to the mean field the PSD scales roughly like  $-5/3$  and  $-2$  in  $R_{\parallel}^1$  and  $R_{\parallel}^2$ , respectively. For perpendicular fluctuations, only a minor difference may be observed between  $R_{\perp}^1$  and  $R_{\perp}^2$  which are characterized by a power-law scaling with index  $-3/2$  and  $-1.57$  in  $R_{\perp}^1$  and  $R_{\perp}^2$ . No clear trend can be observed for  $\alpha_B$  with  $V_{sw}$  and  $\sigma_c$ . The absence of a trend can be attributed either to the relatively long interval duration or to the small sample size, which in this case only included 33 intervals.

A similar picture emerges when considering the local spectral index,  $\alpha_B(\kappa^*)$  obtained by taking a sliding window of size  $w = 3, 5, 10$  in  $\kappa^*$ , over the spectra and calculating the best-fit linear gradient in log-log space over this win-

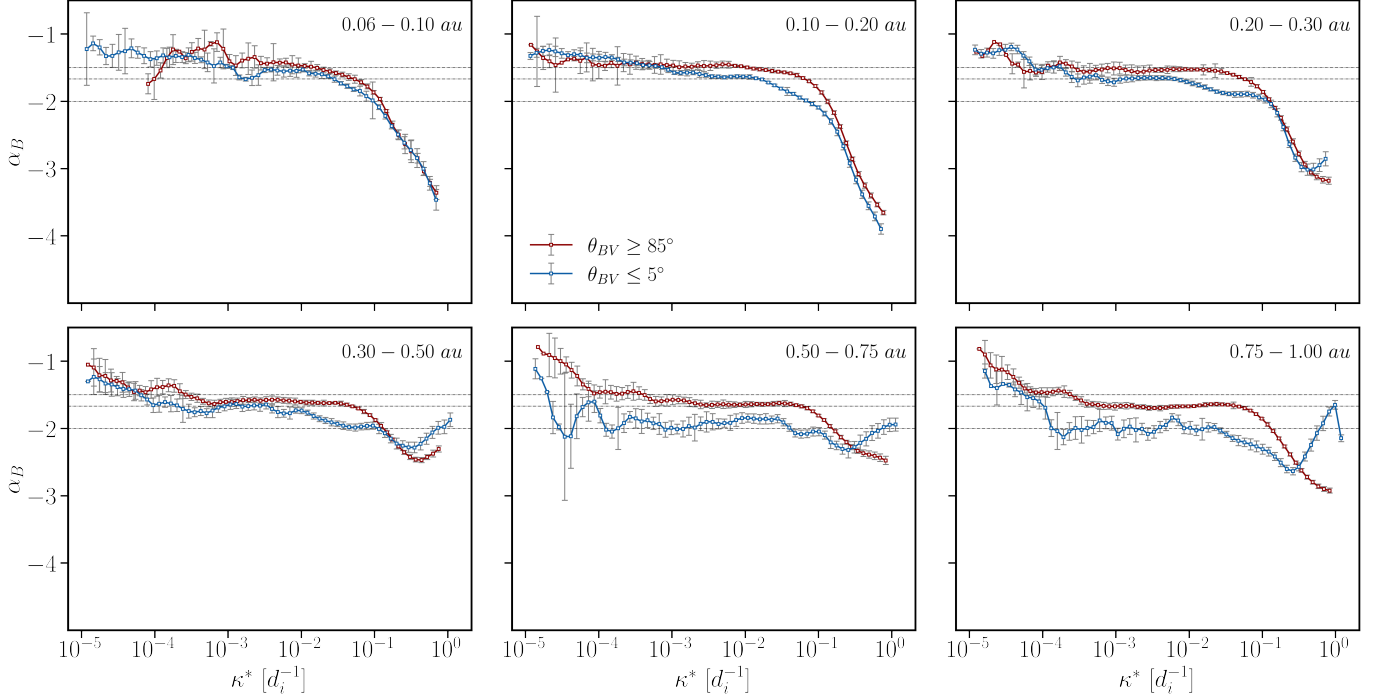


**Figure 3.** The local spectral index ( $\alpha_B(\kappa^*)$ ) for fluctuations with  $\theta_{BV} \leq 5^\circ$  (blue), and  $\theta_{BV} \geq 85^\circ$  (red) at different heliocentric distances for slow streams,  $V_{sw} \leq 400 \text{ km s}^{-1}$ . The local spectral index was calculated for all selected intervals, and each curve corresponds to the mean of all intervals that fall inside the bins indicated in the legend. We focus on MHD scales,  $\kappa d_i \leq 3 \times 10^{-1}$ , because instrumental noise flattens the PSD with increasing distance, as discussed in Section 4.1.

dow is shown in cyan, orange and red respectively in the bottom panel of Figure 1. At the smaller scales,  $\kappa^* \geq 0.1 d_i^{-1}$ , the spectrum steepens between the inertial and kinetic ranges for both parallel and perpendicular fluctuations. A recent analysis of the same dataset by (Duan et al. 2021) found similar transition and inertial range scalings. (Duan et al. 2021), also observe an  $f^{-2}$  scaling in the inertial range of the parallel spectrum extending over  $4 \times 10^{-1} - 2$  Hz. The same scaling is also recovered in our analysis extending over  $R_{\parallel}^1$ . However,  $R_{\parallel}^1$  is not representative of the entire inertial range. More specifically,  $R_{\parallel}^1$ , which in fact occupies the majority of the MHD range, is characterized by a shallower scaling exponent,  $\alpha_B \approx -5/3$ .

We then analyzed the power anisotropy, defined as  $E_{\perp}/E_{\parallel}$  (Podesta 2009), as a function of  $\kappa^*$ . The results of this analysis are displayed in Figure 2, where individual intervals are plotted as scatter points and binned based on their  $\sigma_c$

value. The median curve for each bin is shown and the color of each curve is keyed to  $\sigma_c$ . The median curve (black solid line) in Figure 2 is consistent with previous findings at larger heliocentric distances. Specifically, the curve exhibits a region of near isotropy for  $\kappa d_i \leq 10^{-3}$ , which corresponds to the roll-over to the  $f^{-1}$  range of the magnetic spectrum (see Figure 1). At smaller scales, the anisotropy becomes more pronounced and follows a power-law scaling of  $1/3$ , in accordance with the critical balance conjecture (Sridhar & Goldreich 1994). This  $\kappa^{*1/3}$  scaling is observed within the range of  $4 \times 10^{-2} - 3 \times 10^{-1} [d_i^{-1}]$ , which corresponds to region  $R^2$  in Figure 1. Additionally, while the anisotropy increases at smaller scales until  $\kappa d_i \approx 4 \times 10^{-1}$ , there is a sudden but noticeable local minimum at around  $\kappa d_i \approx 0.7$  followed by a local maximum at  $\kappa d_i \approx 1.7$ . Both the trough and peak are consistently observed across all intervals considered in this study. The local min-



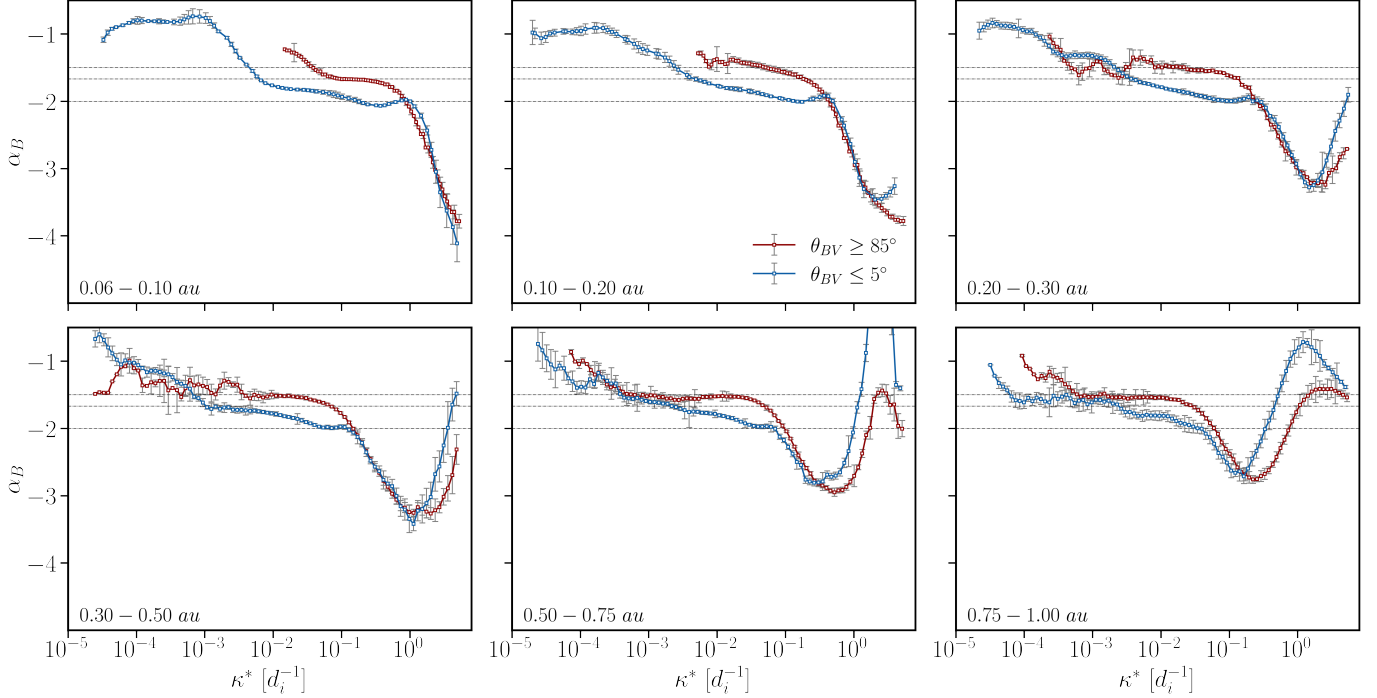


**Figure 4.** The local spectral index ( $\alpha_B(\kappa^*)$ ) for fluctuations with  $\theta_{BV} \leq 5^\circ$  (blue), and  $\theta_{BV} \geq 85^\circ$  (red) at different heliocentric distances for fast streams,  $V_{sw} \geq 400 \text{ km s}^{-1}$ . The local spectral index was obtained for all selected intervals and each curve corresponds to the mean of all the intervals that fall inside the bins indicated in the legend.

imum may be caused by the bump observed in  $E_{\parallel}$  at  $\kappa d_i \approx 0.6$ , which coincides with the beginning of the transition region in  $E_{\perp}$  (see Figure 1). This bump may suggest a local enhancement of energy that could be due to ion kinetic instabilities (Wicks et al. 2010). For a more comprehensive discussion of the double-peak structure in Figure 2a, see (Podesta 2009). The results of this study differ from those of (Podesta 2009) in that we observe an increase in anisotropy at smaller scales  $\kappa d_i > 2$ . As shown in Figure 7 of (Podesta 2009), a rapid decrease in the power ratio is observed beyond the local kinetic scale maximum of approximately 1 Hz, which is attributed to the dissipation of kinetic Alfvén waves (KAWs). However, as the spacecraft moves farther away from the sun, the amplitude of the fluctuations at kinetic scales is close to the noise floor of the magnetometer. This can lead to an artificial steepening of the power spectral density (PSD) caused by instru-

mental noise (Woodham 2019). The effect is particularly significant for  $\alpha_B(\kappa^*)$  parallel, as most of the power in the solar wind is associated with wavevectors polarized perpendicular to the mean magnetic field. As a result, the parallel PSD systematically obtains lower values at MHD and kinetic scales and is therefore more likely to be affected by instrumental noise. On the other hand, the perpendicular PSD can remain intact. This can cause the parallel PSD to flatten out and the power ratio to decrease with decreasing scale. Considering that (1) the aforementioned paper uses magnetic field data from the STEREO mission (Acuña et al. 2008) at Earth-orbit, where the turbulence amplitude is lower compared to that observed by PSP’s E1, and (2) the SCAm data product merges fluxgate and search-coil magnetometer measurements, allowing for magnetic field observations up to 1 MHz with an optimal signal-to-noise ratio, we attribute the discrep-

ancy to instrumental noise that may have affected the parallel PSD in Figure 7 of (Podesta 2009).

To estimate the anisotropy relation between  $\ell_{\parallel}$  and  $\ell_{\perp}$ , we equate the second-order structure functions for parallel and perpendicular fluctuations,  $SF_{\parallel}^2$  and  $SF_{\perp}^2$ , respectively, estimated as

$$SF^2(\ell^*, \theta_{BV}) = \frac{(d_i/V_{SW})}{N} \sum_{n=1}^N \left| \frac{\omega(t_n, \ell, \theta_{BV})}{\sqrt{\ell}} \right|^2. \quad (9)$$

The resulting anisotropy is shown in Figure 2b. In region  $R^2$ , the anisotropy exhibits a power-law scaling with an index of approximately 2/3, consistent with critical balance (Goldreich & Sridhar 1997), indicating that magnetic fluctuations are elongated along the magnetic field. The anisotropy becomes even stronger at smaller scales, where scalings of approximately 5/2 and 2 are observed in the transition and kinetic range, respectively.

#### 4.2. Radial Evolution of anisotropic turbulence

##### 4.2.1. Spectral-index anisotropy

In the following, we investigate the evolution of spectral index anisotropy with heliocentric distance. For this analysis we consider overlapping intervals of duration  $d = 24$  hours sampled by the PSP and SO at distances between 0.06 - 1 au (see Section 3.2). Previous research has shown that the dominant orientation of fluctuation wavevectors in fast solar wind streams tends to be quasi-parallel to the local magnetic field, while in slow solar wind streams the dominant orientation is quasi-perpendicular (Dasso et al. 2005). To investigate the unique characteristics of each type of stream and how they may influence the evolution of anisotropy in the solar wind, we separate our analysis into two groups: slow streams with  $V_{sw} \leq 400 \text{ km s}^{-1}$  and fast streams with  $V_{sw} \geq 400 \text{ km s}^{-1}$ .

We first consider the evolution of slow streams, which constitute the majority of the samples acquired from PSP and SO. For each interval, we calculate the local spectral index, in the direction parallel,  $\theta_{BV} \leq 5^\circ$ , and perpendicular,  $\theta_{BV} \geq 85^\circ$ , to the locally dominant magnetic field, following the process described in Section 4.1 and utilizing a sliding window of size  $w = 10$ . The analysis was repeated for bins of width  $10^\circ$  with similar results. We subsequently divided our intervals into six heliocentric bins and calculated a mean local spectral index for intervals falling within each bin. Despite the fact that the original spectra, as well as the local spectral indices, were calculated at identical frequencies depending on the duration of the interval and the sampling frequency, the normalization process results in a shift along the vertical axis that is irregular. For this reason, the entire range of  $\kappa^*$  was divided into 100 bins, and the mean was calculated for all  $\alpha_B(\kappa^*)$  values falling in each bin, (Němeček et al. 2021). The radial size of each bin is shown in the legend of Figure 3. The slow wind local spectral indices, as a function of heliocentric distance, are shown in blue for perpendicular fluctuations, and in red for parallel fluctuations along with error bars indicating the standard error of the mean. The standard error is given by  $\sigma_i/\sqrt{N}$ , where  $\sigma_i$  is the standard deviation and  $N$  is the number of samples inside the bin, as described in (Gurland & Tripathi 1971). We focus our attention on MHD scales,  $\kappa d_i \leq 3 \times 10^{-1}$ , here simply because instrumental noise artificially steepens the PSD with increasing distance, as discussed in Section 4.1.

It is evident from Figure 3 that the spectral-index anisotropy of slow wind turbulence diminishes closer to the Sun. Within 0.1 au, both parallel and perpendicular spectra are characterized by a poorly developed inertial range, viz. the range of scales over which the spectral index is constant is limited to  $3 \times 10^{-3} \lesssim \kappa d_i \lesssim$

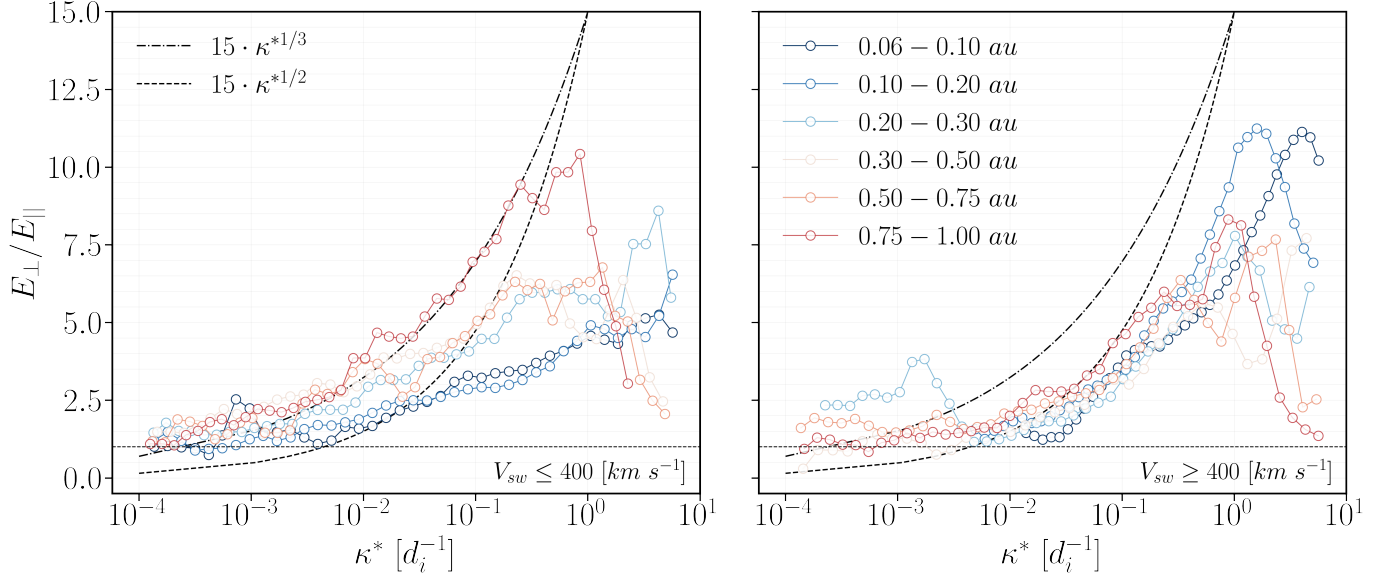


**Figure 5.** The radial evolution of the power anisotropy, represented by the ratio  $E_{\perp}/E_{\parallel}$ , is depicted as a function of heliocentric distance for slow ( $V_{sw} \leq 400 \text{ km s}^{-1}$ ) and fast ( $V_{sw} \geq 400 \text{ km s}^{-1}$ ) streams. Six heliocentric-radius bins were utilized, and each curve represents the median of  $E_{\perp}/E_{\parallel}$  from all intervals that fall within each bin. The dashed ( $y = 15 \cdot \kappa^{*1/2}$ ) and dashed-dotted ( $y = 15 \cdot \kappa^{*1/3}$ ) lines were added as reference points, indicating consistency with “dynamically aligned” and “critically balanced” cascade, respectively.

$2 \times 10^{-2}$  with a scaling exponent  $-1.47 \pm 0.04$  and  $-1.55 \pm 0.05$  for perpendicular and parallel fluctuations. At distances 0.1-0.2 au, two sub-ranges ( $R^1$  and  $R^2$ ) emerge within the inertial range. The transition occurs at  $\kappa d_i \approx 6 \times 10^{-2}$ , and the scaling exponents in these ranges are similar to those shown in Figure 1. However, the steepened region  $R^2$  is not as well defined in this case. Considering that the PSP was at a distance of 0.17 au during E1, we attribute this discrepancy to the fact that  $R^2$  actually appears closer to 0.2 au. By shifting the left boundary of the bin towards 0.2 au, we confirmed this expectation as the steepened region displayed a parallel power-law scaling of -2 when the left boundary was shifted to approximately 0.15 au.

In  $R^1$  both parallel and perpendicular spectra dynamically evolve with increasing distance and steepen towards -5/3, which in the case of the parallel spectrum occurs within 0.1 au. The steepening occurs in a scale-dependent fashion which results in  $R^2$  extending to larger scales with distance. As a result, for distances ex-

ceeding 0.5 au,  $R^1$  practically vanishes, and the power spectra are characterized by a power-law exponent that changes from -5/3 in the direction perpendicular to -2 in the direction parallel to the locally dominant mean field in good agreement with the predictions of “critical balance” theory.

We next examined the evolution of fast streams ( $V_{sw} \geq 400 \text{ km s}^{-1}$ ). However, since all data from PSP and SO were collected in the ecliptic plane during the minimum of the Solar Cycle, there was a limited amount of high-speed wind samples. We, therefore, performed a thorough visual inspection to ensure that only fast streams were included in our analysis. Furthermore, it is important to consider that as the solar wind expands in the heliosphere, the local mean magnetic field vectors become increasingly oriented at larger angles relative to the radial direction. This radial trend causes sampling at 0.06 AU to be more quasi-longitudinal, and sampling at 1.0 AU to be more quasi-perpendicular. As parallel fluctuations decrease

with increasing distance, our ability to accurately estimate the low-frequency part of the parallel power spectrum is reduced. This effect makes the determination of the anisotropic scaling laws for high-speed streams in the ecliptic plane challenging, as there is insufficient data to make accurate measurements at low frequencies. While using longer records could resolve this issue, the limited lifetime of the streams restricts the length of the record. In an effort to address this issue, we imposed a minimum interval length that would allow for a large enough interval size but still enable us to gather a sufficient number of intervals for our statistical study. Specifically, for heliographic distances exceeding 0.3, and 0.5 au, we set the minimum interval size to 12 and 20 hours respectively. This resulted in a total of 274 intervals sampled across the inner heliosphere. The results of this analysis are presented in Figure 4. It is readily seen that the differences between fast and slow intervals are significant. When examining the lower frequencies, we observe that within 0.2 au, the energy injection range of the PSD is dominated by parallel fluctuations. In particular, a remarkably extended and relatively shallow range with  $\alpha_B \approx -0.8$  is observed within 0.1 au, which steepens towards -1 with distance. This is particularly noteworthy as previous research has shown that Alfvén waves (AWs) can parametrically decay into slow magnetosonic waves and counter-propagating AWs (Galeev & Oraevskii 1963; Tenerani et al. 2017; Malara et al. 2022). This process may lead to the development of a  $k_{\parallel}^{-1}$  spectrum for outward-propagating AWs by the time they reach a heliocentric distance of 0.3 au in the fast solar wind (Chandran 2018). For a more comprehensive investigation of the radial evolution of the lower-frequency part of the spectrum, see (Huang et al., submitted to APJ). Due to the issues with interval size that were discussed earlier, we do not attempt to interpret the evolution of the

lower-frequency part of the spectrum beyond 0.3 au.

Focusing on MHD scales, we notice that the perpendicular PSD only extends up to  $\kappa d_i \approx 10^{-2}$ , indicating that fast streams near the Sun are characterized by a strong core, radial field, and a lack of low-frequency, perpendicular fluctuations. Interestingly, within 0.1 au, the scaling of the perpendicular spectrum is consistent with  $-5/3$ , but at larger distances, a scaling that is roughly consistent with  $-3/2$ , fluctuating between -1.49 to -1.55, is observed. This suggests that the MHD range spectral index of the perpendicular spectrum for fast streams may not evolve in a consistent manner with increasing distance in the inner heliosphere. It is worth noting, however, that within 0.1 au, only four intervals with  $V_{sw} \geq 400$  km/s were sampled by PSP. More data from fast streams near the Sun is needed to statistically confirm these findings. For parallel fluctuations, the inertial range scaling remains remarkably similar across all heliographic bins with the spectral index progressively steepening towards smaller scales from  $-5/3$  towards -2, where a narrow range of scales over which the local spectral index obtains a constant value appears. In contrast to slow wind streams, the high-frequency point in fast wind streams does not remain anchored in a normalized wavenumber but gradually drifts towards larger scales with distance. This is an interesting finding that suggests the evolution of the high-frequency point is different between fast and slow wind streams and is discussed further in Section 5.

#### 4.2.2. Power anisotropy

In this section we examine the radial evolution of the power anisotropy, represented by the ratio  $E_{\perp}/E_{\parallel}$ , in fast and slow solar wind intervals. To do this, we utilized the method described in Section 4.2.1 and calculated the mean of  $E_{\perp}/E_{\parallel}$  in six heliocentric bins. The results of this analysis are presented in Figure 5a for slow streams

and Figure 5b for fast streams. According to theories based on “dynamical alignment”, the inertial range scaling index should be  $1/2$  when considering  $E_{\perp}/E_{\parallel}$ , while a slope of  $1/3$  is predicted by theories of “critical balance”.

For slow wind streams, the power anisotropy becomes more significant with increasing distance, particularly at smaller scales (see Figure 5a). This suggests that the turbulence undergoes an anisotropic cascade, transporting the majority of its magnetic energy towards larger perpendicular wavenumbers. In contrast, fast streams show practically no significant radial trend, especially when taking into account the error bars (not shown here). As a result, even though the power anisotropy is more pronounced for fast winds closer to the Sun, at distances of around 1 au, the situation is reversed, and slow wind exhibits higher values of  $E_{\perp}/E_{\parallel}$ . In terms of anisotropic scaling, we observe that  $E_{\perp}/E_{\parallel}$  evolves in a manner similar to what was described in Subsection 4.2.1. Specifically, the scaling of  $E_{\perp}/E_{\parallel}$  for slow wind streams does not fit the predictions of any of the existing anisotropic theories closer to the Sun, but with increasing distance, it evolves towards a scaling that is consistent with CB theories. The situation is more complex for fast streams. In particular, for the bin closest to the Sun, the scaling of  $E_{\perp}/E_{\parallel}$  is closer to that predicted by CB theories ( $\kappa^{*1/3}$ ), but for the rest of the bins, the scaling exponent fluctuates in the range between  $1/2 - 1/3$ . Additionally, the double peak structure discussed in Section 4.1 is also observed for most of the curves in this analysis, especially in fast wind intervals. However, at smaller scales, the curves are strongly affected by instrumental noise, causing the power ratio to decrease.

## 5. DISCUSSION

Wavelet analysis of solar wind data obtained at heliocentric distances greater than 0.3 au has shown strong agreement between the

anisotropic characteristics of magnetic turbulence and the predictions of the “critical balance” conjecture (Horbury et al. 2008; Wicks et al. 2010). However, (Podesta 2009) cautioned that it would be premature to draw conclusions about the agreement of the scaling in the fast solar wind with any particular theory due to the large uncertainties of the scaling at the largest scales. It is worth noting that these studies either focused on high-speed streams or prolonged periods of both high-speed and slow streams (Horbury et al. 2008; Wicks et al. 2010; Wicks et al. 2013; He et al. 2013). When extended intervals are considered, the PSD behavior will be practically determined by the fast sub-intervals since high-speed streams exhibit higher-amplitude magnetic fluctuations. Recent PSP measurements below 0.3 au have provided an unprecedented opportunity to study the nature of the solar wind in the vicinity of the solar wind sources. (Bandyopadhyay & McComas 2021; Adhikari et al. 2022) have recently shown that large-scale fluctuations in the near-Sun solar wind are dominated by wavevectors quasi-parallel to the local magnetic field.

Inertial range spectral anisotropy has been investigated by (Huang et al. 2022; Wu et al. 2022), who used slow solar wind data from E1 of PSP to show that the spectral indices are close to  $-5/3$  and  $-3/2$  in the parallel and perpendicular direction, respectively. (Wu et al. 2022) also compared the anisotropic spectral properties of the slow wind stream sampled by PSP during E1 to a fast wind,  $V_{sw} \approx 770 \text{ km s}^{-1}$ , Ullyses stream at 1.48 au and concluded that the differences between the near-Sun and near-Earth solar wind likely result from the existence of two sub-ranges in the inertial range, with the one closer to kinetic scales ( $\sim 30d_i - 300d_i$ ) displaying a radial steepening, while the one at larger scales remains unchanged. (Wu et al. 2022) also showed that the transition between the two ranges does not evolve radially, but re-



mains constant in  $\kappa d_i$ . However, since fast and slow streams display very different radial evolutions based on turbulence signatures (Shi et al. 2021; Sioulas et al. 2022a,c), the validity of this result remains questionable.

Several significant questions remain to be addressed in regards to the anisotropy of magnetic turbulence in the solar wind and its evolution as it expands into the heliosphere: (1) Does the anisotropy dynamically evolve with distance? (2) Are there differences in spectral and power anisotropy between fast and slow streams, and if so, (3) do these differences evolve with distance? In the following section, we compare our findings with those of previous studies in an effort to address these questions.

## 6. COMPARISON WITH PREVIOUS STUDIES

### 6.1. Comparison with Horbury et al. (2008) & Podesta (2009)

In our study, using data from PSP and SO, we estimated perpendicular inertial range spectral indices for the fast wind with values in the range of  $[-1.49, -1.55]$ . These values are slightly shallower than those reported in previous studies Horbury et al. (2008); Podesta (2009); Wicks et al. (2010), which estimate values in the range of  $[-1.55, -1.67]$ . One possible reason for this discrepancy could be that the PSP and SO data were only collected in the ecliptic plane during the minimum and early rising phase of the Solar Cycle. It is known that solar wind conditions can vary significantly over the course of the Solar cycle, and it is possible that these variations could affect the observed scalings of the perpendicular spectra. In addition, due to the phase of the Solar Cycle, only a limited number of extended fast wind streams were collected. For example, PSP only sampled four intervals with  $V_{sw} \geq 400$  km/s within 0.1 au. This limitation may affect the statistical significance of the results and make it difficult to accurately measure

the anisotropic scaling laws for these streams at lower frequencies. As a result, it may be premature to draw firm conclusions about the agreement of the scaling in the fast solar wind sampled in the ecliptic plane by PSP and SO with any particular theory of anisotropic MHD turbulence.

### 6.2. Comparison with Wicks et al. (2010)

Our results indicate that, when analyzing slow wind streams, normalizing the PSD with  $d_i$  allows us to fix the high-frequency break point,  $f_b$ , in normalized wavenumber space, as previously reported in (Sioulas et al. 2022b). In contrast, for fast solar wind streams,  $f_b$  tends to drift towards larger  $\kappa d_i$  with increasing distance. Statistically, fast solar wind streams are characterized by higher proton temperature ( $T_p$ ) (Maksimovic et al. 2020; Shi et al. 2021; Shi et al. 2023), which result in higher plasma pressure and therefore higher plasma  $\beta$  values, i.e., the ratio of thermal to magnetic pressure,  $\beta \equiv n_p K_B T_p / (B^2 / 2\mu_0) \ll 1$ . Furthermore, (Chen et al. 2014) have shown that the  $f_b$  of the magnetic PSD between inertial and kinetic scales correlates better with  $d_i$  when the intervals are characterized by  $\beta < 1$  values, while high  $\beta$  intervals are characterized by a small scale break at the thermal ion gyroradius ( $\rho_i$ ). In line with this, our analysis confirms the findings of (Wicks et al. 2010), who used five fast solar wind streams with  $\beta > 1$  between 1.5 - 2.8 au and found that the small scale end of the inertial range seems to naturally scale with the ion gyroradius when normalized with  $\rho_i$ . Given that  $\rho_i$  grows radially as  $\propto R^{1.48 \pm 0.02}$  (Sioulas et al. 2022b), we expect that  $f_b$  will display a similar radial trend for fast solar wind streams.

### 6.3. Comparison with Wu et al. (2022)

The use of high-resolution data from E1 of PSP allowed us to confirm the existence of two sub-ranges (Telloni 2022; Wu et al. 2022) within the inertial range. The transition occurs at

$\kappa d_i \approx 6 \times 10^{-2}$  and signifies a shift from  $-5/3$  to  $-2$  scaling in the parallel spectra and from  $-3/2$  to  $-1.57$  scaling in the perpendicular spectra. The difference between the two ranges ( $R^1$ ,  $R^2$ ) is most apparent in the parallel spectrum and could signify a transition from weak to strong turbulence (Sridhar & Goldreich 1994; Meyrand et al. 2016; Zank et al. 2020). It is important to note that the parallel spectral index we report here for  $R_{\parallel}^2$ ,  $\alpha_B \approx -2$ , is steeper than the one reported by Wu et al. (2022). The differences observed in the results are unlikely to be a result of the use of structure functions in the study by Wu et al. (2022), as we utilized second-order structure functions to verify the anisotropic scaling. However, it is possible that the discrepancies may be attributed to the use of higher quality SCA data in our study. Specifically, the parallel structure function in Figure 4b of Wu et al. appears to become steeper at smaller timescales, but the limited cadence of approximately 1 Hz may not allow for the clear observation of such scaling.

Furthermore, we have observed that the anisotropic properties and their dynamic evolution differ significantly between fast and slow streams. In addition to the differences observed in the evolution of the inertial range scaling, we have found that the high-frequency breakpoint shifts to lower frequencies at a faster rate when analyzing fast wind streams. These results contradict the conclusions made by Wu et al. (2022) and suggest that a meaningful comparison can only be made if streams of similar wind speeds are considered.

## 7. CONCLUSIONS & SUMMARY

We used a merged PSP and SO dataset to study the dynamic evolution of turbulence anisotropy in the inner heliosphere, with a focus on understanding the differences in anisotropy observed between fast and slow wind streams

The main findings of our study can be summarized as follows:

For slow wind streams,  $V_{sw} \leq 400 \text{ km s}^{-1}$ , we find:

(a1) Within 0.1 au, the spectral index anisotropy of the inertial range vanishes, and the inertial range is confined to  $3 \times 10^{-3} \lesssim \kappa d_i \lesssim 2 \times 10^{-2}$ . The scaling exponents are  $-1.47 \pm 0.04$  and  $-1.55 \pm 0.05$  for perpendicular and parallel fluctuations, respectively. The power anisotropy ( $E_{\perp}/E_{\parallel}$ ) is weaker compared to previous studies at 1 AU, and its inertial range scaling does not fit any predictions of anisotropic theories of turbulence.

(a2) At  $\approx 0.15$  au two inertial subranges ( $R^1$ ,  $R^2$ ) emerge. The transition occurs at  $\kappa d_i \approx 6 \times 10^{-2}$ , and signifies a shift from  $-5/3$  to  $-2$  and  $-3/2$  to  $\approx -1.6$  scaling in parallel and perpendicular spectra, respectively.

(a3) Beyond this point, the power anisotropy monotonically strengthens with distance, indicating an anisotropic turbulent cascade that transports most of its magnetic energy towards larger perpendicular wavenumbers. Additionally, region  $R^2$  extends towards smaller wavenumbers, gradually "consuming" region  $R^1$ . This process results in a scale-dependent steepening of the inertial range.

(a4) At distances exceeding 0.5 au, region  $R^1$  practically vanishes, and the power spectra are characterized by a power-law exponent that changes from  $-5/3$  in the direction perpendicular to  $-2$  in the direction parallel to the locally dominant mean field in good agreement with the predictions of "critical balance".

(a5) The rate at which the high-frequency breakpoint  $f_b$  of the magnetic power spectrum drifts to lower frequencies with distance scales naturally with the rate at which the ion inertial scale,  $d_i$ , grows with distance. In other words,

the high-frequency point  $f_b$  is observed to remain anchored in  $\kappa d_i$ .

For fast streams,  $V_{sw} \geq 400 \text{ km s}^{-1}$ , we find:

(b1) Closer to the Sun, the energy injection range,  $\kappa d_i \leq 10^{-3}$ , of the spectrum is dominated by parallel fluctuations. Within 0.1 AU, this range exhibits a quite extended shallow region with a scaling index of  $\approx -0.8$ . This region appears to steepen towards -1 with increasing distance, providing evidence for the Parametric decay instability (PDI) as a generating mechanism for the  $k_{\parallel}^{-1}$  spectrum in the fast solar wind (Chandran 2018). For a more detailed discussion see (Huang et al., submitted to APJ).

(b2) In MHD scales, the scaling of both the parallel and perpendicular spectra does not exhibit a clear radial trend. Within 0.1 au, the scaling of the perpendicular spectrum is consistent with  $-5/3$ . Beyond 0.1 AU, the perpendicular spectral index fluctuates between -1.49 and -1.55. For parallel fluctuations, the inertial range scaling remains remarkably similar across all heliographic bins. The spectral index progressively steepens towards smaller scales from  $-5/3$  towards -2, where a narrow range of scales over which the local spectral index obtains a constant value is observed.

(b3) Power-anisotropy for fast streams does not seem to display a clear trend with distance. In terms of inertial range scaling, we find that fast streams are more consistent with (Boldyrev 2006) model based on “dynamical alignment” than (Goldreich & Sridhar 1997) model based on “critical balance” but the large uncertainties at lower frequencies make the statistical significance of this result questionable.

(b4) In agreement with (Wicks et al. 2010), the high-frequency point,  $f_b$  is observed to remain anchored in  $\kappa \rho_i$ .

A deeper understanding of anisotropy could be gained by considering the effect of intermit-

tency on turbulence (Oboukhov 1962), i.e., the concentration of fluctuation energy into smaller volumes of space at smaller scales. Recent research has demonstrated a connection between critical balance and dynamic alignment with intermittency (Chandran et al. 2015; Mallet & Schekochihin 2017). A more comprehensive analysis comparing the anisotropic scaling of higher-order moments to existing theories is in progress.

The analysis of turbulence in the inner heliosphere requires a thorough examination of the applicability of homogeneous turbulence theories and models to the observed characteristics. This is particularly crucial when considering the potential for the Alfvén speed to approach or surpass the solar wind speed. Power anisotropies also necessitate careful examination, as there may be fundamental connections between wave-number couplings and large-scale gradients in both the radial and transverse directions. The solar corona, for instance, may play a significant role in refracting energy in fast-mode polarization into regions of low Alfvén speed or even causing total reflection. These couplings may also impact the spectral slopes in the parallel and perpendicular directions within the nascent solar wind (Velli et al. 1991).

In conclusion, it is important to recognize the potential limitations of the current analysis, including the limited number of extended fast wind streams sampled by PSP and SO. These limitations may affect the statistical significance of the results and make it difficult to accurately determine the anisotropic scaling laws for these streams at lower frequencies. Therefore, it is advisable to continue collecting more samples from PSP and SO, particularly those of longer duration, to confirm the statistical significance of the findings. In addition, a more robust statistical analysis with longer intervals of data from Ulysses and Helios will be conducted to accu-

rately determine the scaling of the anisotropy and its dependence on the heliocentric distance, phase of the solar cycle, and heliographic latitude.

1 This research was funded in part by the  
2 FIELDS experiment on the Parker Solar  
3 Probe spacecraft, designed and developed  
4 under NASA contract NNN06AA01C; the  
5 NASA Parker Solar Probe Observatory Sci-  
6 entist grant NNX15AF34G and the HER-  
7 MES DRIVE NASA Science Center grant No.  
8 80NSSC20K0604. The instruments of PSP were  
9 designed and developed under NASA contract  
10 NNN06AA01C. MV acknowledges the support  
11 of ISSI, Bern, via the Johannes Geiss fellowship.

12 *Software:* Python (Van Rossum & Drake Jr  
13 1995), SciPy (Virtanen et al. 2020), Pandas  
14 (McKinney et al. 2010), Matplotlib (Hunter  
15 2007),

## REFERENCES

- Acuña, M. H., Curtis, D., Scheifele, J. L., et al. 2008, *SSRv*, 136, 203, doi: [10.1007/s11214-007-9259-2](https://doi.org/10.1007/s11214-007-9259-2)
- Adhikari, L., Zank, G. P., Zhao, L.-L., & Telloni, D. 2022, *The Astrophysical Journal*, 933, 56, doi: [10.3847/1538-4357/ac70cb](https://doi.org/10.3847/1538-4357/ac70cb)
- Alberti, T., Laurenza, M., Consolini, G., et al. 2020, *The Astrophysical Journal*, 902, 84, doi: [10.3847/1538-4357/abb3d2](https://doi.org/10.3847/1538-4357/abb3d2)
- Bale, S. D., Goetz, K., Harvey, P. R., et al. 2016, *r*, 204, 49, doi: [10.1007/s11214-016-0244-5](https://doi.org/10.1007/s11214-016-0244-5)
- Bale, S. D., Badman, S. T., Bonnell, J. W., et al. 2019, *Nature*, 576, 237, doi: [10.1038/s41586-019-1818-7](https://doi.org/10.1038/s41586-019-1818-7)
- Bandyopadhyay, R., & McComas, D. J. 2021, *The Astrophysical Journal*, 923, 193, doi: [10.3847/1538-4357/ac3486](https://doi.org/10.3847/1538-4357/ac3486)
- Belcher, J. W., & Davis Jr., L. 1971, *Journal of Geophysical Research* (1896-1977), 76, 3534, doi: <https://doi.org/10.1029/JA076i016p03534>
- Beresnyak, A., & Lazarian, A. 2010, *The Astrophysical Journal*, 722, L110, doi: [10.1088/2041-8205/722/1/L110](https://doi.org/10.1088/2041-8205/722/1/L110)
- Bieber, J. W., Wanner, W., & Matthaeus, W. H. 1996, *Journal of Geophysical Research: Space Physics*, 101, 2511, doi: <https://doi.org/10.1029/95JA02588>
- Biskamp, D. 2003, *Magnetohydrodynamic Turbulence*
- Boldyrev, S. 2006, *Phys. Rev. Lett.*, 96, 115002, doi: [10.1103/PhysRevLett.96.115002](https://doi.org/10.1103/PhysRevLett.96.115002)
- Borovsky, J. E., Denton, M. H., & Smith, C. W. 2019, *Journal of Geophysical Research: Space Physics*, 124, 2406, doi: <https://doi.org/10.1029/2019JA026580>
- Bowen, T. A., Bale, S. D., Bonnell, J. W., et al. 2020, *Journal of Geophysical Research: Space Physics*, 125, e2020JA027813, doi: <https://doi.org/10.1029/2020JA027813>
- Bruno, R., Carbone, V., Sorriso-Valvo, L., & Bavassano, B. 2003, *Journal of Geophysical Research (Space Physics)*, 108, 1130, doi: [10.1029/2002JA009615](https://doi.org/10.1029/2002JA009615)
- Chandran, B. D. G. 2018, *Journal of Plasma Physics*, 84, 905840106, doi: [10.1017/S0022377818000016](https://doi.org/10.1017/S0022377818000016)
- Chandran, B. D. G., & Perez, J. C. 2019, *Journal of Plasma Physics*, 85, 905850409, doi: [10.1017/S0022377819000540](https://doi.org/10.1017/S0022377819000540)
- Chandran, B. D. G., Schekochihin, A. A., & Mallet, A. 2015, *ApJ*, 807, 39, doi: [10.1088/0004-637X/807/1/39](https://doi.org/10.1088/0004-637X/807/1/39)
- Chen, C. H. K., Leung, L., Boldyrev, S., Maruca, B. A., & Bale, S. D. 2014, *Geophys. Res. Lett.*, 41, 8081, doi: [10.1002/2014GL062009](https://doi.org/10.1002/2014GL062009)



- Chen, C. H. K., Mallet, A., Yousef, T. A., Schekochihin, A. A., & Horbury, T. S. 2011, *MNRAS*, 415, 3219, doi: [10.1111/j.1365-2966.2011.18933.x](https://doi.org/10.1111/j.1365-2966.2011.18933.x)
- Chen, C. H. K., Bale, S. D., Bonnell, J. W., et al. 2020, *The Astrophysical Journal Supplement Series*, 246, 53, doi: [10.3847/1538-4365/ab60a3](https://doi.org/10.3847/1538-4365/ab60a3)
- Chhiber, R. 2022, *The Astrophysical Journal*, 939, 33, doi: [10.3847/1538-4357/ac9386](https://doi.org/10.3847/1538-4357/ac9386)
- Dasso, S., Milano, L. J., Matthaeus, W. H., & Smith, C. W. 2005, *ApJL*, 635, L181, doi: [10.1086/499559](https://doi.org/10.1086/499559)
- Davies, L., & Gather, U. 1993, *Journal of the American Statistical Association*, 88, 782, doi: [10.1080/01621459.1993.10476339](https://doi.org/10.1080/01621459.1993.10476339)
- Dong, C., Wang, L., Huang, Y.-M., et al. 2022, *Science Advances*, 8, eabn7627, doi: [10.1126/sciadv.abn7627](https://doi.org/10.1126/sciadv.abn7627)
- Duan, D., He, J., Bowen, T. A., et al. 2021, *The Astrophysical Journal Letters*, 915, L8, doi: [10.3847/2041-8213/ac07ac](https://doi.org/10.3847/2041-8213/ac07ac)
- Elsasser, W. M. 1950, *Phys. Rev.*, 79, 183, doi: [10.1103/PhysRev.79.183](https://doi.org/10.1103/PhysRev.79.183)
- Galeev, A. A., & Oraevskii, V. N. 1963, *Soviet Physics Doklady*, 7, 988
- Galtier, S., Nazarenko, S. V., Newell, A. C., & Pouquet, A. 2000, *Journal of Plasma Physics*, 63, 447, doi: [10.1017/S0022377899008284](https://doi.org/10.1017/S0022377899008284)
- Gerick, F., Saur, J., & von Papen, M. 2017, *The Astrophysical Journal*, 843, 5, doi: [10.3847/1538-4357/aa767c](https://doi.org/10.3847/1538-4357/aa767c)
- Goldreich, P., & Sridhar, S. 1995, *\apj*, 438, 763, doi: [10.1086/175121](https://doi.org/10.1086/175121)
- . 1997, *\apj*, 485, 680, doi: [10.1086/304442](https://doi.org/10.1086/304442)
- Gurland, J., & Tripathi, R. C. 1971, *The American Statistician*, 25, 30. <http://www.jstor.org/stable/2682923>
- He, J., Tu, C., Marsch, E., Bourouaine, S., & Pei, Z. 2013, *The Astrophysical Journal*, 773, 72, doi: [10.1088/0004-637X/773/1/72](https://doi.org/10.1088/0004-637X/773/1/72)
- Higdon, J. C. 1984, *ApJ*, 285, 109, doi: [10.1086/162481](https://doi.org/10.1086/162481)
- Horbury, T. S., Forman, M., & Oughton, S. 2008, *\prl*, 101, 175005, doi: [10.1103/PhysRevLett.101.175005](https://doi.org/10.1103/PhysRevLett.101.175005)
- Horbury, T. S., Wicks, R. T., & Chen, C. H. K. 2012, *\ssr*, 172, 325, doi: [10.1007/s11214-011-9821-9](https://doi.org/10.1007/s11214-011-9821-9)
- Horbury, T. S., O'Brien, H., Carrasco Blazquez, I., et al. 2020, p, 642, A9, doi: [10.1051/0004-6361/201937257](https://doi.org/10.1051/0004-6361/201937257)
- Huang, S. Y., Xu, S. B., Zhang, J., et al. 2022, *The Astrophysical Journal Letters*, 929, L6, doi: [10.3847/2041-8213/ac5f02](https://doi.org/10.3847/2041-8213/ac5f02)
- Hunter, J. D. 2007, *Computing in Science & Engineering*, 9, 90, doi: [10.1109/MCSE.2007.55](https://doi.org/10.1109/MCSE.2007.55)
- Iroshnikov, P. S. 1963, *Astronomicheskii Zhurnal*, 40, 742. <https://ui.adsabs.harvard.edu/abs/1963AZh....40..742I>
- Kasper, J. C., Abiad, R., Austin, G., et al. 2016, r, 204, 131, doi: [10.1007/s11214-015-0206-3](https://doi.org/10.1007/s11214-015-0206-3)
- Klein, K. G., Perez, J. C., Verscharen, D., Mallet, A., & Chandran, B. D. G. 2015, *The Astrophysical Journal*, 801, L18, doi: [10.1088/2041-8205/801/1/L18](https://doi.org/10.1088/2041-8205/801/1/L18)
- Kraichnan, R. H. 1965, *The Physics of Fluids*, 8, 1385
- Lithwick, Y., Goldreich, P., & Sridhar, S. 2007, *ApJ*, 655, 269, doi: [10.1086/509884](https://doi.org/10.1086/509884)
- Maksimovic, M., Bale, S. D., Berčić, L., et al. 2020, *ApJS*, 246, 62, doi: [10.3847/1538-4365/ab61fc](https://doi.org/10.3847/1538-4365/ab61fc)
- Malara, F., Primavera, L., & Veltri, P. 2022, *Universe*, 8, doi: [10.3390/universe8080391](https://doi.org/10.3390/universe8080391)
- Mallet, A., & Schekochihin, A. A. 2017, *MNRAS*, 466, 3918, doi: [10.1093/mnras/stw3251](https://doi.org/10.1093/mnras/stw3251)
- Maron, J., & Goldreich, P. 2001, *ApJ*, 554, 1175, doi: [10.1086/321413](https://doi.org/10.1086/321413)
- Mason, J., Cattaneo, F., & Boldyrev, S. 2006, *Phys. Rev. Lett.*, 97, 255002, doi: [10.1103/PhysRevLett.97.255002](https://doi.org/10.1103/PhysRevLett.97.255002)
- Matteini, L., Horbury, T. S., Neugebauer, M., & Goldstein, B. E. 2014, *Geophysical Research Letters*, 41, 259, doi: <https://doi.org/10.1002/2013GL058482>
- Matthaeus, W. H., Goldstein, M. L., & Roberts, D. A. 1990, *J. Geophys. Res.*, 95, 20673, doi: [10.1029/JA095iA12p20673](https://doi.org/10.1029/JA095iA12p20673)
- McKinney, W., et al. 2010, in *Proceedings of the 9th Python in Science Conference*, Vol. 445, Austin, TX, 51–56
- Meyrand, R., Galtier, S., & Kiyani, K. H. 2016, *Phys. Rev. Lett.*, 116, 105002, doi: [10.1103/PhysRevLett.116.105002](https://doi.org/10.1103/PhysRevLett.116.105002)
- Moncuquet, M., Meyer-Vernet, N., Issautier, K., et al. 2020, *The Astrophysical Journal Supplement Series*, 246, 44, doi: [10.3847/1538-4365/ab5a84](https://doi.org/10.3847/1538-4365/ab5a84)



- Montgomery, D., & Matthaeus, W. H. 1995, *ApJ*, 447, 706, doi: [10.1086/175910](https://doi.org/10.1086/175910)
- Montgomery, D., & Turner, L. 1981, *The Physics of Fluids*, 24, 825, doi: [10.1063/1.863455](https://doi.org/10.1063/1.863455)
- Ng, C. S., & Bhattacharjee, A. 1996, *ApJ*, 465, 845, doi: [10.1086/177468](https://doi.org/10.1086/177468)
- Ně meek, Z., afr á nkov á , J., N ě mec, F., et al. 2021, *Atmosphere*, 12, 1277, doi: [10.3390/atmos12101277](https://doi.org/10.3390/atmos12101277)
- Oboukhov, A. M. 1962, *Journal of Fluid Mechanics*, 13, 77, doi: [10.1017/S0022112062000506](https://doi.org/10.1017/S0022112062000506)
- Osman, K. T., Matthaeus, W. H., Wan, M., & Rappazzo, A. F. 2012, *Phys. Rev. Lett.*, 108, 261102, doi: [10.1103/PhysRevLett.108.261102](https://doi.org/10.1103/PhysRevLett.108.261102)
- Oughton, S., Matthaeus, W. H., Wan, M., & Osman, K. T. 2015, *Philosophical Transactions of the Royal Society A: Mathematical, Physical and Engineering Sciences*, 373, 20140152, doi: [10.1098/rsta.2014.0152](https://doi.org/10.1098/rsta.2014.0152)
- Owen, C. J., Bruno, R., Livi, S., et al. 2020, p, 642, A16, doi: [10.1051/0004-6361/201937259](https://doi.org/10.1051/0004-6361/201937259)
- Parker, E. N. 1979, *Cosmical magnetic fields. Their origin and their activity*
- Perez, J. C., & Boldyrev, S. 2009, *Phys. Rev. Lett.*, 102, 025003, doi: [10.1103/PhysRevLett.102.025003](https://doi.org/10.1103/PhysRevLett.102.025003)
- Pi, G., PitÅa, A., N ě meček, Z., et al. 2020, *SoPh*, 295, 84, doi: [10.1007/s11207-020-01646-8](https://doi.org/10.1007/s11207-020-01646-8)
- Pine, Z. B., Smith, C. W., Hollick, S. J., et al. 2020, *ApJ*, 900, 93, doi: [10.3847/1538-4357/abab11](https://doi.org/10.3847/1538-4357/abab11)
- Podesta, J. J. 2009, *The Astrophysical Journal*, 698, 986, doi: [10.1088/0004-637x/698/2/986](https://doi.org/10.1088/0004-637x/698/2/986)
- Schekochihin, A. A., Cowley, S. C., Dorland, W., et al. 2009, *The Astrophysical Journal Supplement Series*, 182, 310, doi: [10.1088/0067-0049/182/1/310](https://doi.org/10.1088/0067-0049/182/1/310)
- Shebalin, J. V., Matthaeus, W. H., & Montgomery, D. 1983, *Journal of Plasma Physics*, 29, 525547, doi: [10.1017/S0022377800000933](https://doi.org/10.1017/S0022377800000933)
- Shi, C., Velli, M., Panasenco, O., et al. 2021, p, 650, A21, doi: [10.1051/0004-6361/202039818](https://doi.org/10.1051/0004-6361/202039818)
- Shi, C., Velli, M., Lionello, R., et al. 2023, *arXiv e-prints*, arXiv:2301.00852, <https://arxiv.org/abs/2301.00852>
- Sioulas, N., Huang, Z., Velli, M., et al. 2022a, *The Astrophysical Journal*, 934, 143, doi: [10.3847/1538-4357/ac7aa2](https://doi.org/10.3847/1538-4357/ac7aa2)
- Sioulas, N., Huang, Z., Shi, C., et al. 2022b, *Magnetic field spectral evolution in the inner heliosphere*, arXiv, doi: [10.48550/ARXIV.2209.02451](https://doi.org/10.48550/ARXIV.2209.02451)
- . 2022c, *Magnetic field spectral evolution in the inner heliosphere*, arXiv, doi: [10.48550/ARXIV.2209.02451](https://doi.org/10.48550/ARXIV.2209.02451)
- Sridhar, S., & Goldreich, P. 1994, *ApJ*, 432, 612, doi: [10.1086/174600](https://doi.org/10.1086/174600)
- Taylor, G. I. 1938, *Proceedings of the Royal Society of London. Series A - Mathematical and Physical Sciences*, 164, 476, doi: [10.1098/rspa.1938.0032](https://doi.org/10.1098/rspa.1938.0032)
- Telloni, D. 2022, *Frontiers in Astronomy and Space Sciences*, 9, doi: [10.3389/fspas.2022.917393](https://doi.org/10.3389/fspas.2022.917393)
- Telloni, D., Sorriso-Valvo, L., Woodham, L. D., et al. 2021, *ApJL*, 912, L21, doi: [10.3847/2041-8213/abf7d1](https://doi.org/10.3847/2041-8213/abf7d1)
- Tenerani, A., Velli, M., & Hellinger, P. 2017, *ApJ*, 851, 99, doi: [10.3847/1538-4357/aa9bef](https://doi.org/10.3847/1538-4357/aa9bef)
- Van Rossum, G., & Drake Jr, F. L. 1995, *Python reference manual (Centrum voor Wiskunde en Informatica Amsterdam)*
- Vasquez, B. J., Smith, C. W., Hamilton, K., MacBride, B. T., & Leamon, R. J. 2007, *Journal of Geophysical Research: Space Physics*, 112, doi: <https://doi.org/10.1029/2007JA012305>
- Velli, M. 1993, *A&A*, 270, 304
- Velli, M., Grappin, R., & Mangeney, A. 1991, *Geophysical & Astrophysical Fluid Dynamics*, 62, 101, doi: [10.1080/03091929108229128](https://doi.org/10.1080/03091929108229128)
- Virtanen, P., Gommers, R., Oliphant, T. E., et al. 2020, *Nature Methods*, 17, 261, doi: [10.1038/s41592-019-0686-2](https://doi.org/10.1038/s41592-019-0686-2)
- Weygand, J. M., Matthaeus, W. H., Dasso, S., et al. 2009, *Journal of Geophysical Research: Space Physics*, 114, doi: <https://doi.org/10.1029/2008JA013766>
- Wicks, R. T., Horbury, T. S., Chen, C. H. K., & Schekochihin, A. A. 2010, *mnras*, 407, L31, doi: [10.1111/j.1745-3933.2010.00898.x](https://doi.org/10.1111/j.1745-3933.2010.00898.x)
- Wicks, R. T., Mallet, A., Horbury, T. S., et al. 2013, *Phys. Rev. Lett.*, 110, 025003, doi: [10.1103/PhysRevLett.110.025003](https://doi.org/10.1103/PhysRevLett.110.025003)
- Woodham, L. 2019, *PhD thesis*, doi: [10.13140/RG.2.2.21508.45443](https://doi.org/10.13140/RG.2.2.21508.45443)

Wu, H., He, J., Yang, L., et al. 2022, On the scaling and anisotropy of two subranges in the inertial range of solar wind turbulence, arXiv, doi: [10.48550/ARXIV.2209.12409](https://doi.org/10.48550/ARXIV.2209.12409)

Zank, G. P., Nakanotani, M., Zhao, L.-L., Adhikari, L., & Telloni, D. 2020, The Astrophysical Journal, 900, 115, doi: [10.3847/1538-4357/abad30](https://doi.org/10.3847/1538-4357/abad30)

Zank, G. P., Zhao, L. L., Adhikari, L., et al. 2022, ApJL, 926, L16, doi: [10.3847/2041-8213/ac51da](https://doi.org/10.3847/2041-8213/ac51da)